Correspondence to:
F. Němec,
frantisek.nemec@gmail.com

Characterizing Average Electron Densities in the Martian Dayside Upper Ionosphere

F. Němec[1] , **D. D. Morgan[2]** , **A. J. Kopf[2]**, **D. A. Gurnett[2]** , **D. Pitoňák[1]**, **C. M. Fowler[3]**, **D. J. Andrews[4]** , and **L. Andersson[5]**

[1]Faculty of Mathematics and Physics, Charles University, Prague, Czech Republic, [2]Department of Physics and Astronomy, University of Iowa, Iowa City, IA, USA, [3]Space Sciences Laboratory, University of California, Berkeley, CA, USA, [4]Swedish Institute of Space Physics, Uppsala, Sweden, [5]Laboratory for Atmospheric and Space Physics, University of Colorado Boulder, Boulder, CO, USA

Abstract We use more than 10 years of the Martian topside ionospheric data measured by the Mars Advanced Radar for Subsurface and Ionosphere Sounding radar sounder on board the Mars Express spacecraft to derive an empirical model of electron densities from the peak altitude up to 325 km. Altogether, 16,044 electron density profiles obtained at spacecraft altitudes lower than 425 km and at solar zenith angles lower than 80° are included in the analysis. Each of the measured electron density profiles is accurately characterized by the peak electron density, peak altitude, and three additional parameters describing the profile shape above the peak: (i) steepness at high altitudes, (ii) main layer thickness, and (iii) transition altitude. The dependence of these parameters on relevant controlling factors (solar zenith angle, solar irradiance, crustal magnetic field magnitude, and Sun-Mars distance) is evaluated, allowing for a formulation of a simple empirical model. Mars Atmosphere and Volatile EvolutioN Extreme Ultraviolet monitor data are used to show that the solar ionizing flux can be accurately approximated by the F10.7 index when taking into account the solar rotation. Electron densities predicted by the resulting empirical model are compared with electron densities locally evaluated based on the Mars Advanced Radar for Subsurface and Ionosphere Sounding measurements, with the Langmuir Probe and Waves electron density measurements on board the Mars Atmosphere and Volatile EvolutioN spacecraft, and with electron densities obtained by radio occultation measurements. Although the electron densities measured by the Langmuir Probe and Waves instrument are systematically somewhat lower than the model electron densities, consistent with former findings, the model performs reasonably well.

Plain Language Summary The ionosphere of Mars is the ionized part of its atmosphere, on the dayside ultimately controlled by the solar irradiation. Information about the electron density in there can be, among others, obtained by the radar sounding from a spacecraft orbiting the planet. Such measurements have been performed since 2005 by the Mars Advanced Radar for Subsurface and Ionosphere Sounding on board the Mars Express spacecraft, and they provide us with electron density profiles from the spacecraft altitude down to the altitude of the peak electron density. We use more than 10 years of such measurements to develop an empirical model of typical ionospheric electron densities. The obtained results are compared with electron densities measured in situ by the Langmuir Probe and Waves instrument on board the MAVEN spacecraft available since 2014. A reasonable agreement between the model predictions and these independent observations is found. Finally, the analysis of solar radiation measured by Extreme Ultraviolet monitor on board the MAVEN spacecraft is used to show that, when the solar rotation is properly accounted for, the solar ionizing flux at Mars can be surprisingly well approximated by the solar radio flux measured at Earth.

1. Introduction

There is a significant and ever growing amount of electron density data from the Martian dayside ionosphere. Three principally different methods of measurements are used. First, radio occultation experiments can be used to derive electron density profiles, that is, electron densities as a function of the altitude, spanning the altitudes both below and above the peak altitude. These were performed using the Mariner 9 spacecraft (Kliore et al., 1972a, 1972b; Withers, Weiner, et al., 2015), Mars Global Surveyor spacecraft (Hinson et al.,

1999), Mars Express spacecraft (Grandin et al., 2014; Pätzold et al., 2005), and recently using the Mars Atmosphere and Volatile EvolutioN (MAVEN) spacecraft (Withers et al., 2018). The main disadvantage of these profiles is that their spatial coverage is restricted by geometric constraints imposed by the orbits of Earth and Mars (Tyler et al., 2001; Withers et al., 2005).

The second possible type of measurements is direct in situ measurements of electron/ion densities. Historically, a couple of such profiles was obtained by Viking 1 and 2 landers (Hanson & Zuccaro, 1977). Local electron densities can be also evaluated from the plasma oscillation excited during Mars Advanced Radar for Subsurface and Ionosphere Sounding (MARSIS) radar sounding on board the Mars Express spacecraft (Duru et al., 2008). Finally, the MAVEN spacecraft recently provides both local neutral and ion (Mahaffy et al., 2015) and electron (Andersson et al., 2015) density measurements. Importantly, the in situ electron density measurements can be accompanied by local measurements of other relevant quantities (temperature, plasma composition, and magnetic field), which may facilitate their interpretation. On the other hand, the altitudinal coverage is intrinsically limited by the spacecraft orbit, so that altitudes below the spacecraft periapsis are never sampled. Additionally, considering that the spacecraft never moves vertically down/up, it is principally impossible to obtain electron density profiles—the position of the spacecraft will change along with the spacecraft altitude.

The last possible option for measuring ionospheric electron densities is the usage of a radar sounding. In case of Mars, such measurements were performed by the MARSIS instrument on board the Mars Express spacecraft, which allowed for a topside ionospheric sounding (Gurnett et al., 2005). This provides us with electron density profiles spanning from the spacecraft altitude down to the altitude of the peak electron density. Although the interpretation of electron densities measured in this way is not entirely straightforward (Morgan et al., 2013; Němec, Morgan, & Gurnett, 2016), they represent arguably the most favorable data set for the specification of global morphologies (Mendillo et al., 2013). Note, however, that only electron densities at altitudes above the peak altitude can be measured by the topside ionospheric sounding.

When attempting to characterize ionospheric electron densities, one can try to numerically simulate the entire system (Chaufray et al., 2014; Gonzalez-Galindo et al., 2013; Matta et al., 2015). Alternatively, one may try to benefit from the large electron density data set and basic understanding of processes involved in the ionospheric formation to construct empirical models which fit the observations with a reasonable precision. In the photochemically controlled region close to the peak altitude, where the plasma transport is negligible (Mendillo et al., 2017a; Withers, 2009), such models typically make use of a classical Chapman, (1931a, 1931b) theory, which is found to perform surprisingly well (Gurnett et al., 2005, 2008; Morgan et al., 2008; Vogt et al., 2017). This was used by Mendillo et al. (2013), along with nearly 113,000 peak electron density values obtained by the MARSIS instrument between 2005 and 2012, to develop a model of peak electron densities characterized by the solar zenith angle (SZA), orbital distance, and F10.7 index as a proxy for the solar ionizing flux. The analysis was later extended by Mendillo et al. (2018) to incorporate as many as 215,818 peak electron density values from the years 2005–2015. Sánchez-Cano et al. (2013) used the same parametrization and a combined data set of 1,200 MARSIS radar sounding profiles and 500 Mars Global Surveyor occultation profiles to construct a model of electron densities describing not only the main M2 ionospheric layer but also the lower M1 layer (Fallows et al., 2015a, 2015b; Fox & Weber, 2012; Fox & Yeager, 2009). Němec et al. (2011) used 30,283 MARSIS radar sounding profiles and almost 200,000 local electron density measurements to develop an empirical model of electron densities above the peak altitude, which assumes a Chapman dependence at altitudes below about 200 km (photochemically controlled region) and smoothly transits to an exponential dependence at altitudes above about 325 km (diffusion-controlled region). The model performance at altitudes higher than about 200 km was later improved by incorporating dependences on crustal magnetic field magnitude and solar ionizing flux (Němec, Morgan, Gurnett, & Andrews, 2016).

The ionosphere of Mars is known to exhibit periodicities related to the solar rotation (Nielsen et al., 2006; Rao et al., 2014), and its variability as a function of the solar cycle was also reported (Sánchez-Cano et al., 2015; Withers, Vogt, et al., 2015). Crustal magnetic fields can also influence the electron densities, in particular at high altitudes (Andrews et al., 2014; Němec, Morgan, Gurnett, & Andrews, 2016). In this regard, it may often prove useful and sufficient to analyze total electron content of the ionosphere in place of electron density profiles (Dubinin et al., 2016; Mendillo et al., 2017b), which may be at times easier to evaluate (Safaeinili

et al., 2007). Empirical models of total electron content as a function of relevant controlling parameters were subsequently developed (Mendillo et al., 2017a) and validated (Mendillo et al., 2018).

We use the MARSIS radar sounding data to derive a new formulation of an empirical electron density model at the Martian dayside ionosphere. Making use of a "shape function," each electron density profile is accurately characterized by only five parameters. This allows for a fast convenient calculation of an average electron density profile under given conditions, which can be, among others, used to identify exceptional events and to analyze the influence of parameters unaccounted for in the model by removing the main systematic trends. The model is further validated by electron densities measured in situ both by the MARSIS instrument and by the Langmuir Probe and Waves (LPW) instrument on board the MAVEN spacecraft. The used data sets are described in section 2. A way to accurately characterize topside ionospheric electron density profiles is described in section 3. Section 4 demonstrates that the $F10.7$ index can be used as a reasonable proxy for the solar ionizing flux. A simple empirical model of the dayside ionosphere is then formulated in section 5, and section 6 demonstrates its performance using independent data sets. The obtained results are discussed in section 7, and they are briefly summarized in section 8.

2. Data Set

The MARSIS radar sounder in the ionospheric sounding mode uses 160 quasi-logarithmically spaced frequencies from 0.1 to 5.5 MHz ($\Delta f/f \approx 0.02$). The reflections of the sounding signal from the ionosphere are recorded in 80 equally spaced time delay bins over an interval of 7.31 ms. A detailed description of the MARSIS instrument was given by Jordan et al. (2009), Orosei et al. (2015), and Picardi et al. (2004). The measured intensities of detected echoes as a function of the sounding frequencies f and time delays Δt are then digitized to obtain the $\Delta t(f)$ dependences (Morgan et al., 2013). These can be "inverted" to obtain electron density profiles from the spacecraft altitude down to the peak altitude using standardized inversion techniques (Morgan et al., 2008, 2013).

A principal problem that one has to deal with when performing the inversion is the low power of the sounding signal at low sounding frequencies, which generally prevents the detection of electron densities lower than about $10^4 cm^{-3}$ (Němec et al., 2010). Consequently, an empirical electron density profile shape between the spacecraft altitude (where the electron density can be evaluated from local plasma oscillations, see, e.g., Duru et al., 2008) and the altitude corresponding to the lowest electron density detectable by the ionospheric sounding (typically about 200–220 km) has to be assumed. This necessarily introduces an ambiguity in the inversion process, and different electron density profiles are obtained depending on the profile shape assumed in the density region unaccessible by the ionospheric sounding. This issue was considered in detail by Němec, Morgan, and Gurnett (2016), who derived an improved trace inversion method based on realistic electron density profile shapes in the data gap region. These profile shapes incorporate a change of the profile slopes related to the transition between the photochemical and diffusion regions, and they smoothly connect the locally evaluated plasma number density and higher densities at lower altitudes in such a way that the measured time delay at the lowest detectable sounding frequency is matched. This improved trace inversion routine, along with the values of appropriate parameters and ionospheric quality trace selection criteria derived by Němec et al. (2017), will be used in the present analysis. Considering that electron density profiles are available up to the spacecraft altitude, we further use only the electron density profiles obtained at spacecraft altitudes higher than 325 km, ensuring that the altitudes from the peak altitude up to 325 km are covered. Additionally, in order to minimize the altitudinal region where the radar sounding data are not available and the derived profile has to rely on an empirical shape, only the data measured at spacecraft altitudes lower than 425 km are used in the present study. Altogether, 16,044 MARSIS electron density profiles measured between August 2005 and October 2015 at SZAs lower than 80° are included in the analysis.

We note that although the determination of the exact altitudes may be rather challenging due to the aforementioned uncertainty of the electron density profile shape in the data gap region, the shapes of electron density profiles at higher electron densities (lower altitudes) are mostly unaffected by these minor tweaks, and they represent a rather robust data product. Similarly, the peak electron densities obtained by the MARSIS instrument are in principle directly measured (as the maximum sounding frequency yet reflected by the ionosphere). In this regard, one should be, however, aware of the discrete sounding frequency steps of the instrument, which result in the very ends of the ionospheric traces not observed by MARSIS. Although this is partly suppressed by a requirement of the time delay at the maximum frequency of the ionospheric trace
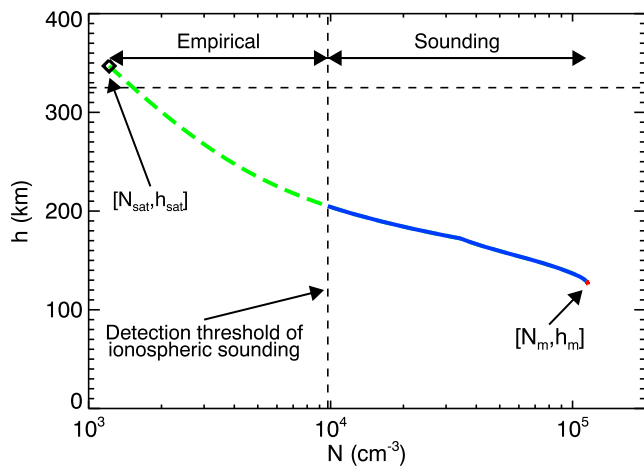
Figure 1. Example of an electron density profile obtained by the Mars Advanced Radar for Subsurface and Ionosphere Sounding topside ionospheric radar sounding. The data were measured on 20 February 2008 at 18:23:43 UT when the spacecraft was located at an altitude of 347 km and solar zenith angle of 40.35°. Electron density at the spacecraft location is evaluated from the locally excited plasma oscillations. The electron density profile from the spacecraft altitude down to the peak altitude is obtained from the ionospheric sounding. However, due to the low power emitted at low sounding frequencies, only the blue part of the profile was obtained from the ionospheric trace; the green-dashed part of the profile corresponds to the assumed empirical electron density profile shape (Němec et al., 2017). The horizontal-dashed line at the altitude of 325 km corresponds to the upper altitude threshold considered in the present study. The vertical-dashed line at an electron density of about 10^4 cm^{-3} shows the detection threshold of the ionospheric sounding for this particular profile. The very end of the ionospheric profile at largest electron densities shown by the red curve was obtained by an extrapolation assuming the Chapman profile shape.

to be larger than the time delay at the sounding frequency just below (Němec et al., 2017), the parts of the electron density profiles in the very vicinity of the ionospheric peak are still missing. Considering the relative sounding frequency steps $\Delta f/f \approx 0.02$, along with the frequency bandwidths of the sounding pulse and the reception channel, we can estimate that the peak frequencies are on average underestimated by less than about 1%. As the electron density is proportional to the square of the plasma frequency, this translates to the underestimation of the peak electron densities by less than about 2%. Analogically, depending on the exact shape of the electron density profile, this also necessarily leads to overestimating the peak altitudes, as the very ends of the electron density profiles close to the peak altitude are not detected by MARSIS. We account for this issue by considering Chapman fits to the very ends of the electron density profiles and using them to effectively extrapolate the profiles down to the peak altitude.

An example of an electron density profile evaluated using an ionospheric trace measured by the MARSIS instrument is shown in Figure 1. The corresponding data were measured on 20 February 2008 at 18:23:43 UT, when the spacecraft was located at an altitude of 347 km and SZA of 40.35°. Electron density N_{sat} at the spacecraft altitude h_{sat} is evaluated from local electron plasma oscillations excited by the MARSIS sounding (Duru et al., 2008). Then, electron densities N at altitudes h spanning from the spacecraft altitude h_{sat} down to the altitude h_m of the peak electron density are in principle obtained from the radar sounding. However, due to the detection threshold of the ionospheric sounding of about 10^4 cm^{-3} (marked by the vertical-dashed line), the upper part of the ionospheric profile shown by the green-dashed curve is not obtained from the sounding itself, but it rather relies on the aforementioned empirical profile shape. Only the higher density part of the profile, shown by the blue color, is obtained from the ionospheric sounding. We note, however, that due to the trace inversion procedure, the exact shape of this part of the profile still depends to some extent on the profile shape at higher altitudes (Morgan et al., 2013). The very end of the profile in Figure 1 shown by the red curve was obtained from the extrapolation down to the peak altitude assuming the Chapman profile shape. Most importantly, this extrapolation ensures that $dN/dh(h_m) = 0$.

Statistical dependences of electron densities derived using the MARSIS radar sounding data will be compared to electron densities locally evaluated from electron plasma oscillations excited by the MARSIS sounding (Andrews et al., 2013; Andrews, Edberg, et al., 2015; Duru et al., 2008, 2010). These represent arguably the most precise electron density measurements, with an accuracy of about ±2% (Duru et al., 2008), but their altitudinal coverage is limited by the periapsis altitude of the Mars Express orbit to altitudes higher than about 275 km. Further, these measurements cannot be performed in regions with high plasma velocities (solar wind and magnetosheath), because the excited wave packet is swept away by the plasma flow (Duru et al., 2008). This may impose a high-altitude limit on the measurements, which, however, does not affect our study limited to low altitudes. Altogether, more than 13,000 electron densities at SZAs lower than 80° locally evaluated based on MARSIS measurements will be used for the comparison.

The statistical dependences obtained from the radar sounding will be further compared with electron densities measured in situ by the LPW instrument onboard the MAVEN spacecraft, whose periapsis altitude is about 150 km (and as low as 125 km during "deep dip" campaigns; Jakosky et al., 2015). The LPW instrument consists of two independent Langmuir probes which measure the current-voltage (I–V) dependence, one after the other in time. Electron densities are obtained by fitting the I–V curves. As the surface properties of the two probes are slightly different, the electron densities obtained from the two probes exhibit minor differences. In order not to be distracted by this, only the data from boom 1 are used in the present study, as recommended by the LPW instrument team. A more detailed description of the LPW instrument was given by Andersson et al. (2015). Altogether, more than 400,000 LPW electron density measurements at
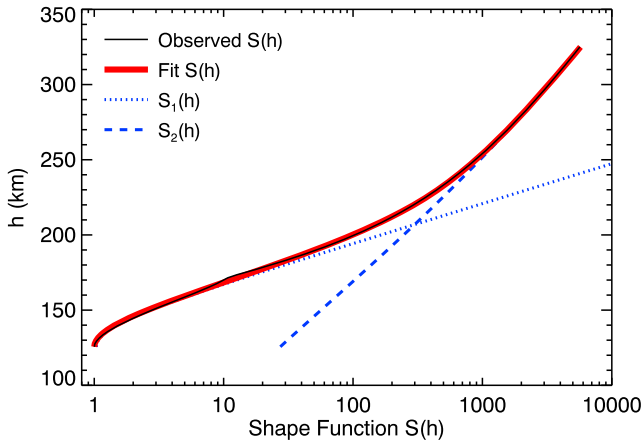
Figure 2. Shape function corresponding to the example profile from Figure 1 as a function of the altitude is shown by the black curve. The red curve shows the fit of the shape function obtained as a combination of the blue dotted and dashed dependences (see text for more details).

altitudes lower than 325 km and at SZAs lower than 80° obtained between October 2014 and January 2017 will be used for the comparison. Note that while more in situ electron density measurements are available at higher altitudes, we limit our analysis only to altitudes lower than 325 km, which are adequately covered by the radar sounding. Electron densities at higher altitudes are known to exhibit significant turbulence-like fluctuations (Andrews, Andersson, et al., 2015; Gurnett et al., 2010), and, moreover, their average dependence can be conveniently described by a simple exponential (Andrews, Edberg, et al., 2015; Duru et al., 2008; Němec et al., 2011).

Finally, electron density profiles obtained by radio occultation measurements at SZAs lower than 80° will be used for comparison. Altogether, 4,100 such electron density profiles obtained by Mars Global Surveyor (4,034), Mars Express (7), and MAVEN (59) spacecraft were used. This represents more than 300,000 electron density data points obtained at altitudes lower than 325 km with relative errors lower than 20%. Unfortunately, their vast majority ($\approx$98%) was measured in a narrow SZA interval between about 70° and 80°.

3. Profile Characterization

Following Nsumei et al. (2012), we describe each of the measured electron density profiles by the peak electron density N_m, peak altitude h_m, and shape function $S(h)$:

$$N(h) = \frac{N_m}{\sqrt{S(h)}} \exp\left\{ \frac{1}{2}\left[1 - Y - \exp(-Y)\right] \right\}, \tag{1}$$

where

$$Y = \frac{1}{h_m} \int_{h_m}^{h} \frac{dh}{S(h)}. \tag{2}$$

Knowing the electron density profile $N(h)$, it is possible to solve for the corresponding shape function $S(h)$ (Nsumei et al., 2012). This shape function, along with the peak altitude and density, fully describes the electron density profile. Thus, instead of trying to describe electron density profiles themselves, we will rather focus on describing the appropriate shape functions. This allows for a convenient mathematical description of the smooth transition from a Chapman profile shape to a different profile slope (Reinisch et al., 2004, 2007; Triskova et al., 2007). The idea is demonstrated in Figure 2. It shows the shape function $S(h)$ corresponding to the example electron density profile from Figure 1 by the black curve. The value of the shape function at the peak altitude is by definition equal to 1, in order to obtain $N(h_m) = N_m$ according to equation (1). At higher altitudes, the shape function monotonically increases. Its typical shape corresponding to the transition between the photochemically dominated Chapman region at low altitudes and the transport-dominated region at higher altitudes (Němec et al., 2011) can be conveniently described as a combination of two functions (Nsumei et al., 2012):

$$\frac{1}{S(h)} = \frac{1}{S_1(h)} + \frac{1}{S_2(h)}, \tag{3}$$

where $S_1(h)$ and $S_2(h)$ are the blue dotted and dashed curves from Figure 2, respectively. These can be described by the following analytical functions (Nsumei et al., 2012):

$$S_1(h) = c_1 \cosh^2\left(\frac{z-1}{\beta/h_m}\right), \tag{4}$$

$$S_2(h) = c_2 \frac{(1+z^2)^\alpha}{z}, \tag{5}$$

where $z = h/h_m$, β corresponds to the main layer thickness (larger values of β correspond to thicker main layers), α corresponds to the steepness of the electron density profile (smaller values of α correspond to steeper electron density profiles), and c_1 and c_2 are constants to be determined from boundary conditions.
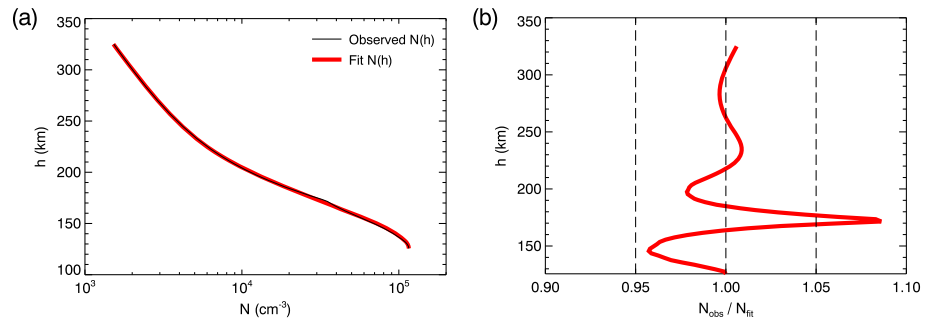
Figure 3. (a) The black curve shows the original electron density profile from Figure 1. The red curve shows the fit electron density profile obtained using the fitted shape function from Figure 2. (b) Ratio between the measured and fitted electron densities as a function of the altitude. The vertical-dashed lines correspond to −5%, exact match, and +5% deviations, respectively.

The values of coefficients c_1 and c_2 are determined in such a way that (i) $S(h_m) = 1$ and (ii) $S_1(h_T) = S_2(h_T)$, where h_T is a "transition altitude" parameter, corresponding to the altitude where the two blue curves from Figure 2 intersect. In this regard, the main layer thickness parameter β is roughly proportional to the neutral scale height close to the peak altitude, and the steepness coefficient α is roughly inversely proportional to the diffusion scale height at high altitudes, that is, at altitudes higher than approximately the transition altitude h_T.

For each electron density profile, the peak electron density N_m, the peak altitude h_m, and the shape function $S(h)$ are evaluated. The best fit parameters α, β, and h_T corresponding to a given shape function are then found. Consequently, each of the electron density profiles measured by MARSIS can be described by only five parameters (peak altitude and density and the three aforementioned parameters used to fit the shape function). In turn, the electron density profile corresponding to these parameters can be rather straightforwardly reconstructed, as the form adopted for $S(h)$ allows the equation (2) to be analytically integrated (Nsumei et al., 2012). The resulting $Y(h)$ is then introduced, along with the evaluated value of the shape function $S(h)$ and peak electron density N_m, into equation (1) to obtain the electron density $N(h)$ at an altitude h.

The performance of the used approach on the example electron density profile from Figure 1 is demonstrated in Figure 3. The black curve in Figure 3a shows the original electron density profile. The red curve shows the electron density profile evaluated using the five characteristic parameters, that is, peak electron density N_m, peak altitude h_m, steepness at high altitudes α, main layer thickness β, and transition altitude h_T. For the example profile, the values of respective parameters are $N_m = 1.16 \times 10^5 \, \text{cm}^{-3}$, $h_m = 125.6 \, \text{km}$, $\alpha = 4.7$, $\beta = 23.0 \, \text{km}$, and $h_T = 206.9 \, \text{km}$. It can be seen that the fitted red electron density profile corresponds very well the original black profile obtained from the MARSIS radar sounding. The differences between the red and black curves are investigated more in detail in Figure 3b, which shows the ratio between the observed and fitted electron densities as a function of the altitude. The vertical-dashed lines correspond to −5% deviation, exact match, and +5% deviation. The differences are typically with about 5%, with an exception of the spike at altitudes of about 170 km. Comparing with Figure 3a, it can be seen that the spike corresponds to the sharp nonsmooth profile feature at these altitudes. Considering that this feature is possibly not real but rather a trace selection/inversion artifact, and, moreover, taking into account that our main aim is to characterize global smooth electron density variations, the differences between the fit and model profiles are very minor. We note that at the peak altitude, the fitted and measured electron densities are by definition exactly equal.

Having demonstrated the performance of the profile characterization on the example profile, we verify its performance on all the 16,044 electron density profiles from our data set. The obtained results are shown in Figure 4. It shows the obtained ratios between observed and fitted electron densities as a function of the altitude above the peak altitude. The total number of events in each altitude-density ratio bin is color coded according to the scale on the right-hand side. The measured electron density profiles were interpolated to a 1-km altitudinal resolution, and the model electron density profiles were evaluated at the very same altitudes. The scale used for the density ratio on the abscissa is logarithmic, principally corresponding to decibel. The bin size used for the density ratio used on the abscissa is 0.1 dB. The solid white nearly vertical curves correspond to 0.25 quartile, median, and 0.75 quartile. It can be seen that the fitted electron densities are
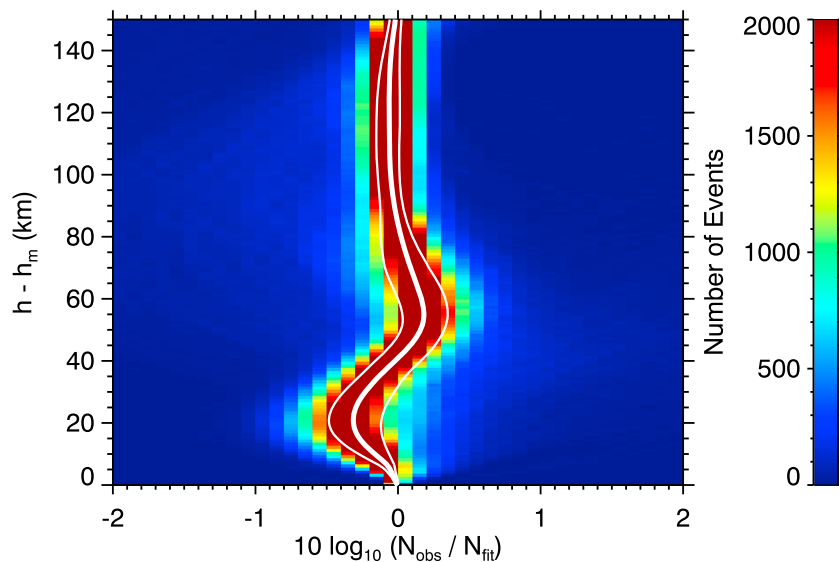
Figure 4. Ratios between the observed and fitted electron densities as a function of the altitude above the peak altitude. Number of events in each altitude-density ratio bin is color coded according to the color scale on the right. The solid white nearly vertical curves correspond to 0.25 quartile, median, and 0.75 quartile, respectively.

within about 20% from the observed densities in the vast majority of events. We note that, similarly as in Figure 3, the ratio between the observed and fitted electron densities at the peak altitude is equal to 1 by definition. We also note that the ratio between the observed and fitted electron densities at higher altitudes seems to exhibit a rather systematic variation, being typically lower than one at altitudes within about 40 km above the peak and being larger than one at altitudes between about 40 and 80 km above the peak. This is related to the empirical approximation used to fit the shape function, which exhibits small but systematic deviations from the real (data-derived) shapes. However, considering the large variation from profile to profile and, most importantly, the inaccuracies in characterizing the profile parameters discussed hereinafter, this simple and computationally very efficient approximation is well sufficient. Following Nsumei et al. (2012), we calculate an average percentage error for each of the analyzed profiles, and we exclude the profiles with average fit errors larger than 20%, which are indicative of problematic trace inversions and/or shape function fits. This removes about 7% of the profiles and leaves us with 14,896 well-fitted profiles for further analysis.

Histograms of the fitted parameters α, β, and h_T obtained for individual electron density profiles are shown in Figures 5a–5c, respectively. It can be seen that the distributions of all the three parameters are roughly symmetric and Gaussian-like, which is advantageous for their further characterization. In order to eliminate extreme and potentially problematic fits with extraordinary parameter values, we disregard electron density profiles with any of the fitted parameters in the lowest or highest 2.5%. The corresponding thresholds applied for individual fitted parameters are shown by the red vertical-dashed lines. The reason for this is that although these extreme values of fit parameters may result in technically good electron density profile fits in terms of the resulting chi-square, the parameters are far from their expected typical values. The profile behavior at the very ends of the fitted interval may be thus undesirable, and, moreover, the extreme values of the obtained parameters would complicate the envisaged further processing. Altogether, there were 13,262 electron density profiles (about 89%) with all the fit parameters within the allowed bounds. These profiles will be included in the further processing, with the aim to statistically characterize the dependences of the fit parameters on relevant controlling factors.

Figure 5d demonstrates how the parameters α, β, and h_T affect the resulting profile shape. We used a fixed peak altitude $h_m = 130$ km, and we plotted the electron densities normalized by the peak electron density (N/N_m) on the abscissa, which effectively eliminates the N_m parameter. The individual profiles were obtained for different combinations of parameter values. The black profile was obtained for median parameter values, that is, $\alpha = 4.9$, $\beta = 23.3$ km, and $h_T = 206.2$ km. The red, green, and blue profiles were then obtained by varying the parameters α, β, and h_T, respectively. The dashed profiles were obtained for
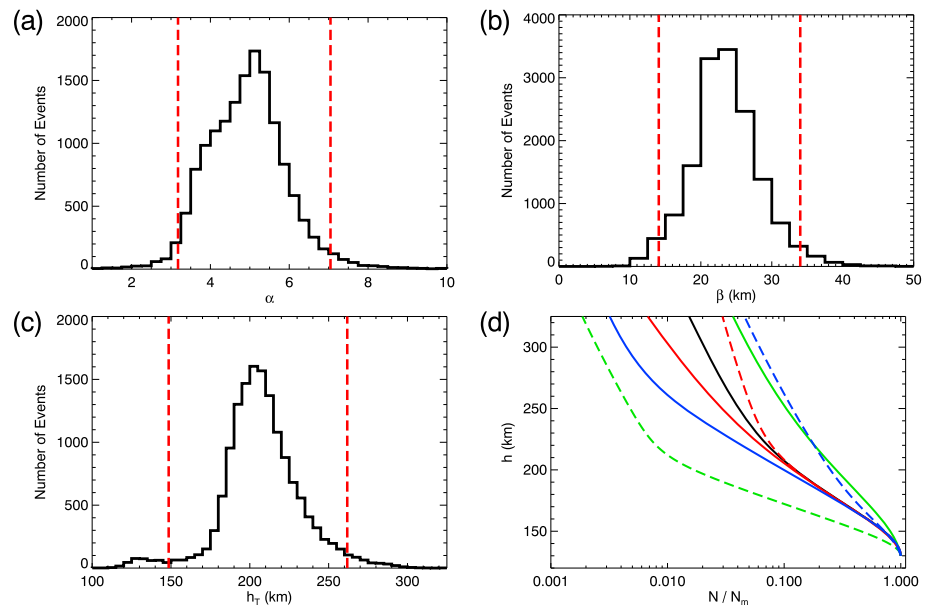
Figure 5. (a–c) Histograms of the obtained fitted values of parameters characterizing the shape function. (a) Steepness at high altitudes α. (b) Main layer thickness β. (c) Transition altitude h_T. The red vertical-dashed lines mark the parameter thresholds, corresponding to the lowest 0.025 and the highest 0.975 percentiles, below/above which the fits are rather extreme and not considered in the further analysis. (d) The influence of the parameters α, β, and h_T on the profile shape. The red, green, and blue profiles were then obtained by varying the parameters α, β, and h_T, respectively. The dashed and solid profiles were obtained for "extremely low" and "extremely high" parameter values, respectively.

"extremely low" parameter values, corresponding to the vertical-dashed lines on the left in Figures 5a–5c. The solid profiles were obtained for "extremely high" parameter values, corresponding to the vertical-dashed lines on the right in Figures 5a–5c.

4. F10.7 as a Proxy for Solar Ionizing Flux

In order to reasonably characterize peak electron densities in the Martian ionosphere, it is important to have a reliable way how to describe the incoming solar irradiance, which is ultimately responsible for the formation of the dayside ionosphere. Many former works have used the F10.7 index as a reasonable proxy. The main advantage of using F10.7 is that it is readily and continuously available. On the other hand, there are two important drawbacks that one should consider: (i) F10.7 values express the power of the solar radio flux, and its correlation with the power at short wavelengths responsible for the ionization has to be assumed, and (ii) F10.7 is measured at Earth, and its recalculation to the Mars location can be problematic. As for the different radial distance, one can take advantage of the radiation power decreasing with the square of the radial distance. However, for the azimuthal distance, the situation is more complicated. Due to the fact that Sun, Earth, and Mars are generally not aligned, the usage of F10.7 values measured at the time of interest necessarily results in the used values being measured at different azimuth with respect to the Sun. This was typically overcome by considering the solar rotation and F10.7 values measured at the correct Sun azimuth (i.e., the azimuth which is in line with Mars at a given time of interest), but at a time somewhat before or after (Morgan et al., 2008). Girazian and Withers (2013) showed that the difference between the results obtained using the real measured solar irradiance and those obtained using the F10.7 proxy can be considerable.

The Extreme Ultraviolet (EUV) monitor instrument on board the MAVEN spacecraft (Eparvier et al., 2015) measurements are routinely used to derive model solar irradiance at Mars with a daily resolution in time and 1-nm resolution in wavelength (Thiemann et al., 2017). We use this MAVEN Level-3 data product to estimate the total solar ionizing flux by summing the spectra over the wavelength range from 5 to 90 nm (Mendillo et al., 2017a), and we investigate its relation with F10.7 index. The obtained results are shown in Figure 6. The total solar ionizing flux derived from the MAVEN EUV data is plotted as a function of F10.7. Each data point corresponds to a single day, spanning from October 2014 to February 2018. Figure 6a was obtained by considering the F10.7 value at the day of the measurement accounting for the Sun-Mars distance. It can be
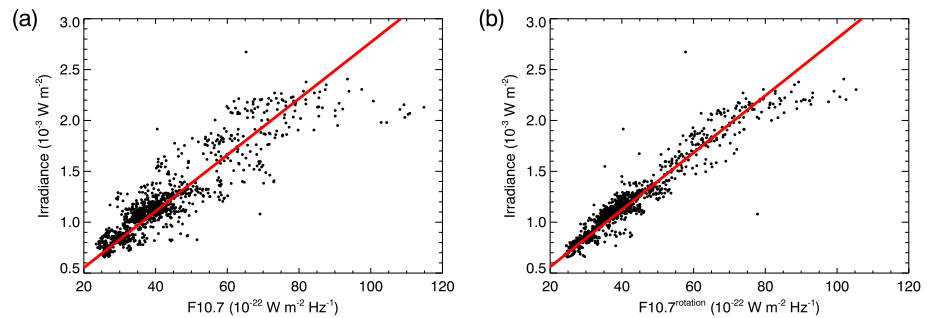
Figure 6. (a) Total solar ionizing flux based on Mars Atmosphere and Volatile EvolutioN Extreme Ultraviolet spacecraft measurements as a function of the F10.7 index at the observation time. The red line corresponds to the best fit linear dependence. (b) The same as (a) but using the F10.7 calculated as a weighted average of the value before and after, accounting for the solar rotation.

seen that the two quantities correlate rather well (the value of the correlation coefficient is about 0.90), but the scatter around the linear dependence is rather large. Moreover, at high values of F10.7, the total solar irradiance based on MAVEN remains quite constant while F10.7 increases.

Figure 6b was obtained by accounting for the solar rotation and using a weighted average of F10.7 measured at a correct solar azimuth just before and just after the time of interest. It can be seen that this procedure results in a significant improvement. Specifically, the scatter around the mean linear dependence is noticeably lower, and the correlation coefficient increases to about 0.96. At high F10.7 values (F10.7 $\gtrsim$ $80 \times 10^{-22} \, \text{W} \cdot \text{m}^{-2} \cdot \text{Hz}^{-1}$), the total solar irradiance remains principally constant while F10.7 increases, roughly consistent with former results (Hantsch & Bauer, 1990; Withers, Morgan, et al., 2015). We thus suggest to replace the F10.7 values larger than $80 \times 10^{-22} \, \text{W} \cdot \text{m}^{-2} \cdot \text{Hz}^{-1}$ by exactly $80 \times 10^{-22} \, \text{W} \cdot \text{m}^{-2} \cdot \text{Hz}^{-1}$. We note, however, that the number of these data points is rather low. Overall, we can conclude that, despite the obvious drawbacks, F10.7 obtained by accounting for the solar rotation is on average a surprisingly good approximation for the total solar irradiance, and its usage for ionospheric empirical models is thus well justified.

5. Empirical Model Based on MARSIS Data

Having characterized each electron density profile by its peak electron density and altitude and the three additional shape parameters, an empirical model of electron densities can be constructed by describing the dependences of these parameters on relevant controlling factors. Given that the dependences of the peak electron density and altitude were already reported by several former studies (e.g., Mendillo et al., 2013; Němec et al., 2011; Sánchez-Cano et al., 2013), we focus primarily on the shape parameters, which are novel to the approach reported in the present paper. Anyway, for the sake of completeness, exactly the same analysis is performed for all the five parameters characterizing each electron density profile.

The following variables are considered as possible controlling factors for each of the fitted parameters: SZA, Sun-Mars distance R in Astronomical Units (AU), F10.7 index recalculated to Mars location taking into account the solar rotation, and magnetic field magnitude B in nanotesla at an altitude of 400 km evaluated using Cain et al. (2003) magnetic field model. The idea is to use a linear regression analysis in order to express the dependences of individual fit parameters on relevant controlling factors. This intrinsically assumes a linear dependence of the fit parameters on the controlling factors. Such a dependence can be, nevertheless, at least roughly achieved by an appropriate transformation of the controlling factors. Specifically, we used a logarithm of Chapman grazing incidence function Ch in place of SZA, one over Sun-Mars distance squared ($1/R^2$) in place of the Sun-Mars distance, logarithm of F10.7 index in place of F10.7 index, and logarithm of the magnetic field magnitude in place of the magnetic field magnitude. In order to identify relevant controlling factors, a rank correlation analysis is applied. First, it is used to determine the most important factor controlling a given fit parameter. This dependence is then expressed by a linear regression, and absolute values of rank correlations between the remaining controlling factors and fit parameter residuals are evaluated. If any of them is higher than 0.1, the appropriate controlling factor is included in the linear regression analysis on top of the factors considered previously, and all the procedure is repeated. Eventually, the absolute values of all rank correlations between the controlling factors and fit parameters are lower than 0.1.
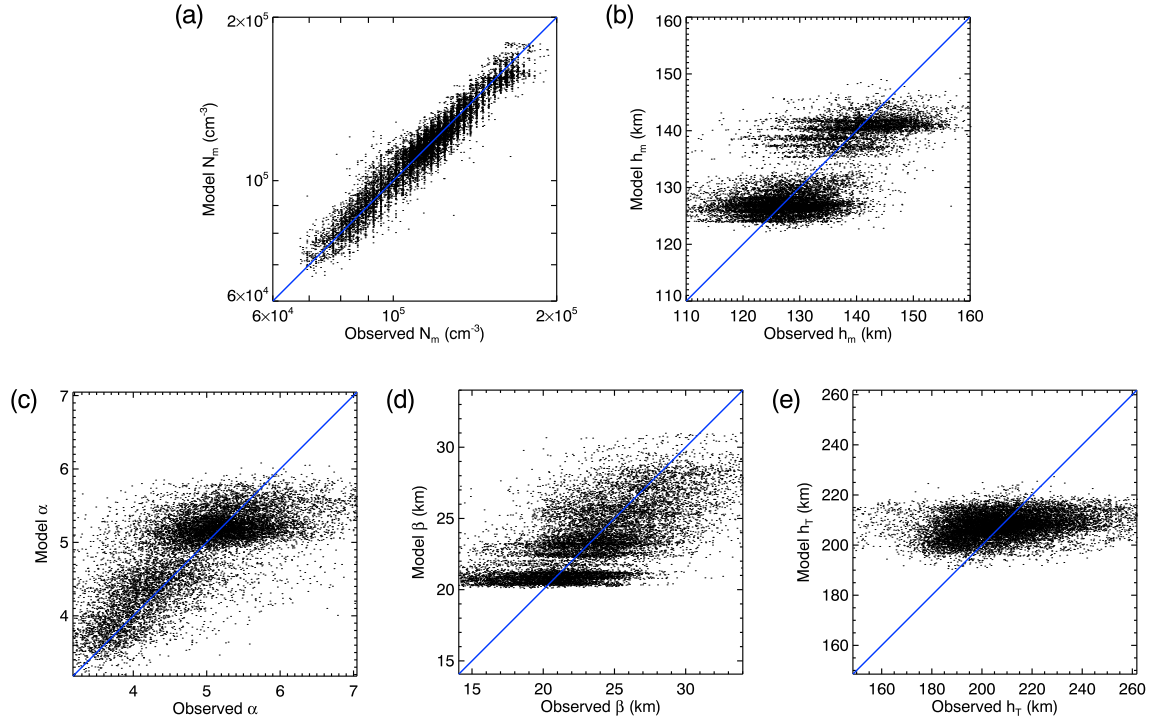
Figure 7. The performance of the suggested parametrization of individual parameters. Model parameter values are plotted as a function of the observed parameter values. The blue lines correspond to a 1:1 dependence. (a) Peak electron density. (b) Peak altitude. (c) Profile slope at high altitudes α. (d) Main layer thickness β. (e) Transition altitude h_T.

The following dependences between the controlling factors and fit parameters were obtained:

$$\ln N_m = 10.537 - 0.490 \ln Ch + 0.370 \ln F10.7 + 0.209/R^2, \tag{6}$$

$$h_m = 105.2 + 5.57 \ln Ch + 115.4/R^2 - 7.08 \ln F10.7, \tag{7}$$

$$\alpha = 5.492 - 0.938 \ln Ch + 4.160/R^2 - 0.151 \ln B - 0.434 \ln F10.7, \tag{8}$$

$$\beta = 0.197 + 6.096 \ln F10.7 + 2.488 \ln Ch, \tag{9}$$

$$h_T = 196.7 - 4.7 \ln B + 44.9/R^2. \tag{10}$$

Note that the parameters are not all dependent on each controlling factor. For example, only the steepness of the electron density profile at high altitudes α and the transition altitude h_T, which represent the electron density profile shape above the main layer, depend on the magnetic field magnitude B. This is consistent with the magnetic field magnitude effects close to the peak altitude being negligible (Němec, Morgan, Gurnett, & Andrews, 2016) but indeed important at higher altitudes (Andrews, Edberg, et al., 2015; Flynn et al., 2017). Additionally, as the Sun-Mars distance R and the $F10.7$ index recalculated to the Mars location are clearly related to each other, the dependence of some of the parameters (β and h_T) is sufficiently described by only one of them, although they are effectively correlated with both.

The performance of these parameter dependences derived from the linear regression analysis is checked in Figure 7. It shows the model parameter values (i.e., the parameter values calculated using equations (6)–(10) as a function of the observed parameter values. The blue lines correspond to 1:1 dependences. Figure 7a shows that the suggested parametrization performs very well in case of peak electron
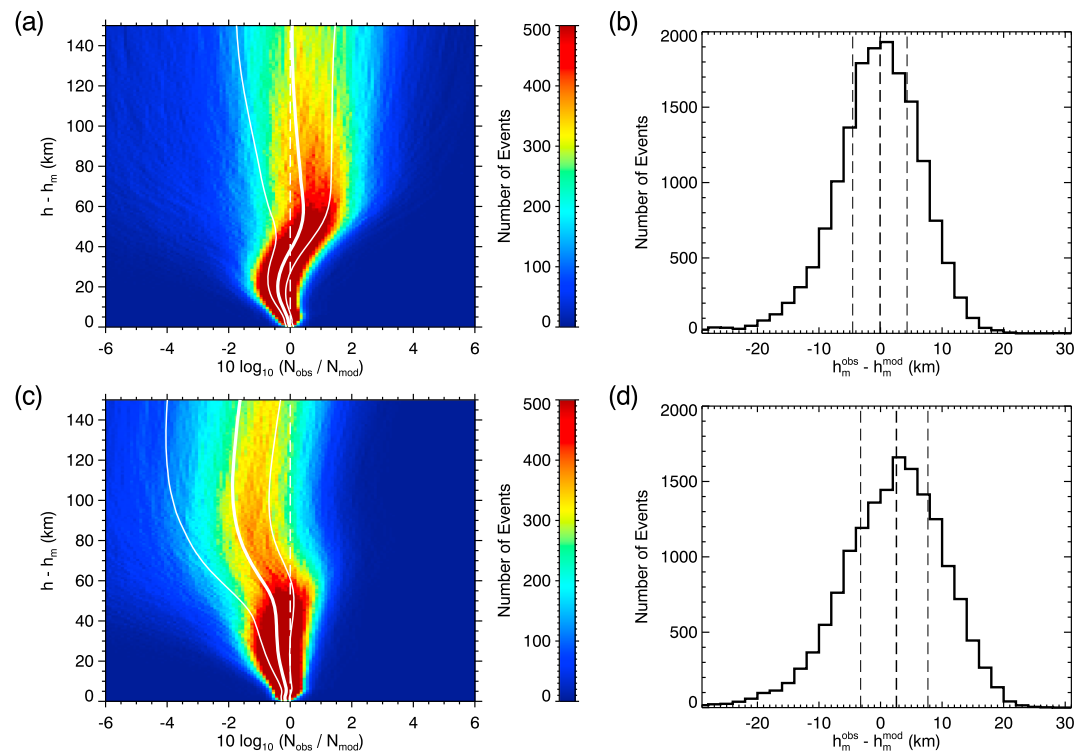
Figure 8. (a) Ratios between the observed and model electron densities as a function of the altitude above the peak altitude. Number of events in each altitude-density ratio bin is color coded according to the color scale on the right. The nearly vertical white curves correspond to 0.25 quartile, median, and 0.75 quartile dependences, left to right, respectively. The vertical-dashed line corresponds to a 1:1 dependence. (b) Histogram of differences between the observed and model peak altitudes. The vertical-dashed lines correspond to 0.25 quartile, median, and 0.75 quartile, left to right, respectively. (c and d) The same as (a) and (b) but for the model by Němec et al. (2011).

density N_m, where the correlation coefficient is as high as 0.96. Note that the vertical stripes apparent in the figure are due to the discrete frequencies of the radar sounding. Figures 7b–7d demonstrate that the performance of the parametrization in case of the peak altitude h_m, the slope at high altitudes α, and the main layer thickness β is worse but still quite reasonable. The appropriate correlation coefficients are equal to 0.71, 0.72, and 0.63, respectively. Finally, the parametrization performs rather poorly for the transition altitude h_T shown in Figure 7e, where the correlation coefficient between the model and observed values is as low as about 0.27. Unfortunately, no better parametrization was found, as the transition altitude h_T is nearly independent on all considered controlling factors. We note that the bimodal distribution apparent in some of the model parameters (in particular h_m, but to some extent also α and β) is due to a bimodal distribution of Sun-Mars distances at the times of MARSIS measurements. Specifically, most MARSIS electron density profiles included in the analysis were obtained at Sun-Mars distances lower than 1.45 AU (about 36%) or larger than 1.60 AU (about 58%). This results in a bimodal distribution also in the F10.7 index recalculated to the Mars location.

Having found the empirical relations that allow us to evaluate, separately for each electron density profile, the model values of profile parameters N_m, h_m, α, β, and h_T, we have in principle constructed an empirical model of ionospheric electron densities. The performance of this empirical model is investigated in Figures 8a and 8b. The total data set of 16,044 electron density profiles is used for the comparison, that is, also the profiles with originally not so good fits are included, necessarily somewhat increasing the scatter. Figure 8a shows a distribution of the ratios between observed and model electron densities (abscissa) as a function of the altitude above the peak altitude (ordinate). In order to allow for a representation as a function of the altitude relative to the peak altitude, we have considered the exact value of the peak altitude (Němec, Morgan, Gurnett, & Andrews, 2016), that is, only the peak electron density N_m and the profile shape parameters α, β, and h_T were determined based on empirical relations (6) and (8)–(10). The format of the figure is the same as that of Figure 4. The white vertical-dashed line corresponds to the 1:1 dependence, that is,
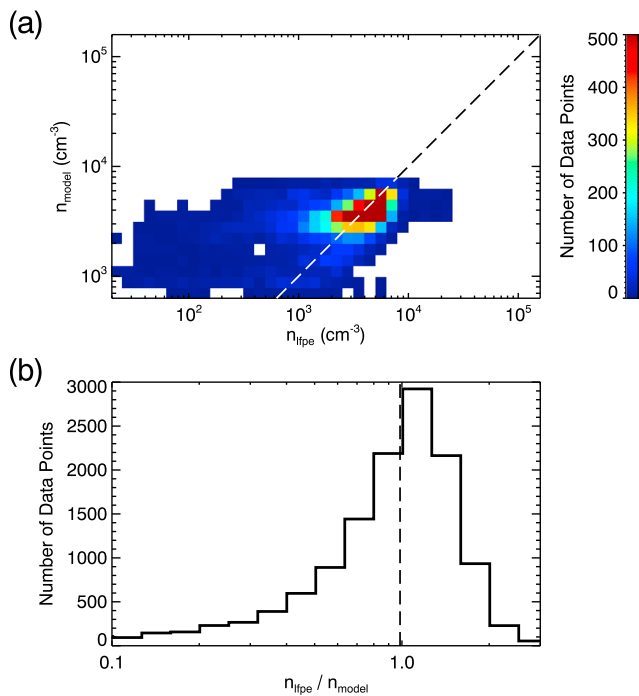
Figure 9. (a) Comparison of model electron densities and electron densities locally evaluated by the Mars Advanced Radar for Subsurface and Ionosphere Sounding instrument. Number of data points in individual logarithmically sized bins is color coded according to the color scale on the right. The black/white-dashed line shows a 1:1 dependence. (b) Histogram of the ratio between electron densities locally evaluated by the Mars Advanced Radar for Subsurface and Ionosphere Sounding instrument and model electron densities. The vertical-dashed line corresponds to the median.

to a situation of an ideal model performance. The scatter of the observed density ratios increases toward higher altitudes, but, importantly, the median value of the density ratio remains rather close to 1 all over the analyzed altitudinal range. The deviations at the highest analyzed altitudes are typically within about ± 1.5 dB, that is, within about 30–40%. A histogram of the differences between the observed and model peak altitudes is shown in Figure 8b. The vertical-dashed lines correspond to 0.25 quartile, median, and 0.75 quartile, left to right, respectively. It can be seen that the peak altitudes are typically within about 5 km from the observed ones.

For the sake of comparison, the same analysis method was used to verify the performance of the formerly developed empirical model (Němec et al., 2011; Němec, Morgan, Gurnett, & Andrews, 2016) in Figures 8c and 8d. It can be seen that the density ratio scatter of this model is somewhat larger than that of the recently suggested model, and, moreover, it exhibits a systematic bias toward higher model electron densities at high altitudes, consistent with the findings by Vogt et al. (2016). This possibly partly stems from the model formulation, but it is definitely also related to the old inversion method used for obtaining electron density profiles for this model, as will be discussed more in detail in section 7.

6. Comparison With Other Data Sets

Having constructed the empirical model of the topside ionospheric densities based on the MARSIS radar sounding data set, it is of interest to compare its results with other available electron density measurements. This is particularly important as the evaluation of electron density profiles from the MARSIS radar sounding has to rely on additional assumptions and empirical profile shapes at higher altitudes (Morgan et al., 2013; Němec, Morgan, & Gurnett, 2016; Němec et al., 2017). A comparison of the model performance with local electron densities evaluated based on electron plasma oscillations excited by MARSIS (Duru et al., 2008) is shown in Figure 9. For each local electron density measurement, we used equations (6)–(10) to get the model parameters N_m, h_m, α, β, and h_T and calculated the model electron density at the spacecraft altitude. Figure 9a then shows the model electron densities as a function of measured electron densities for all the analyzed local electron density measurements. Number of data points in each $0.1 \times 0.1 \log \mathrm{cm}^{-3}$ bin is color coded according to the color scale on the right-hand side. The black/white diagonal-dashed line corresponds to a 1:1 dependence. It can be seen that although the scatter of the data points is rather large, most of them occur reasonably close to the line. One can see that, occasionally, the measured electron densities are significantly lower than the model electron densities. In fact, although electron densities on the order of $10 \, \mathrm{cm}^{-3}$ are at times observed, model electron densities do not get below about $10^3 \mathrm{cm}^{-3}$. This behavior is related to the distribution of electron densities at the considered altitudes and to the fact that the model attempts to describe a typical situation, that is, it ultimately fails at describing extreme electron density values. Additionally, the MARSIS radar sounding assumes the density to monotonically increase with decreasing altitude, and, given the data gap at low sounding frequencies, it effectively detects the first high density value. It is thus unable to see density inhomogeneities and turbulence-like fluctuations common at higher altitudes (Andrews, Andersson, et al., 2015; Gurnett et al., 2010), providing us with a typical density value which is often larger than the real one because the MARSIS signal reflects off the largest density in the region. The correlation between the model and observed electron densities is about 0.50. We note, however, that all the MARSIS local electron densities included in the analysis were measured in a narrow altitudinal range between about 275 and 325 km, that is, the otherwise important altitudinal variation of electron densities is effectively quite small in this case. A histogram of the ratios of observed and model electron densities is shown in Figure 9b. The vertical-dashed line shows the median of the distribution, which is equal to about 0.99. We note that the distribution is not entirely symmetric but has a rather long tail toward low density ratios, in agreement with the results depicted in Figures 8a and 9a.
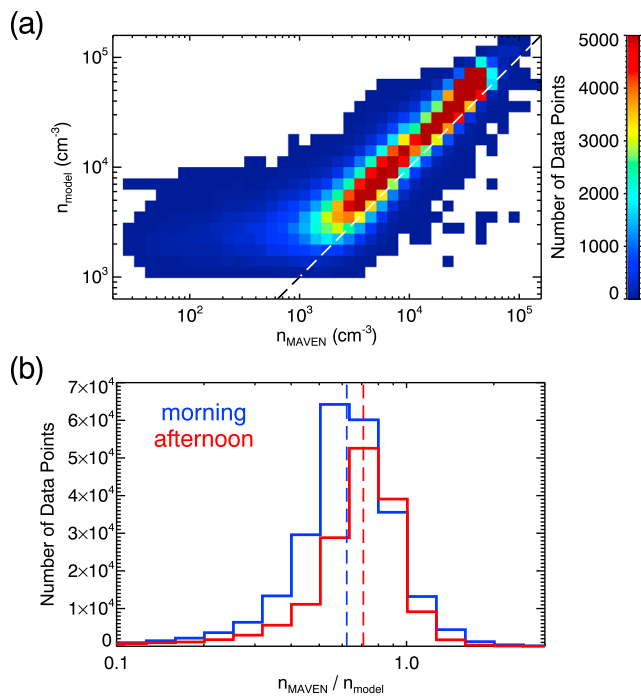
(a)

(b)

Figure 10. (a) Comparison of model electron densities and electron densities locally evaluated by the Langmuir Probe and Waves instrument on board Mars Atmosphere and Volatile EvolutioN. Number of data points in individual logarithmically sized bins is color coded according to the color scale on the right. The black/white-dashed line shows a 1:1 dependence. (b) Histograms of the ratios between electron densities locally evaluated by the Langmuir Probe and Waves instrument and model electron densities. The blue and red histograms correspond to the morning and afternoon local time sectors, respectively. The blue- and red-dashed vertical lines correspond to the median values.

Although electron densities locally evaluated from the MARSIS measurements are determined very precisely, the data coverage is limited by the spacecraft periapsis only to altitudes higher than about 275 km. An additional comparison of model and measured electron densities was thus performed with local electron density measurements performed by the LPW instrument on board the MAVEN spacecraft (Andersson et al., 2015), which samples the altitudes down to about 150 km. Model electron densities as a function of electron densities measured by MAVEN are shown in Figure 10a. The figure uses the same format as Figure 9a. It can be seen that although the model and observed electron densities correlate well, the model electron densities are systematically somewhat larger than those measured. Additionally, similarly to the results obtained for MARSIS locally evaluated electron densities, measured electron densities can be at times by an order of magnitude lower than the model ones, in particular for lower electron densities (higher altitudes). This scatter significantly decreases at higher electron densities (lower altitudes), as might be expected for a more steady photochemically controlled ionosphere. The correlation between the observed and model electron densities is about 0.95. A distribution of the ratios between the measured and model electron densities is shown in Figure 10b. While the MARSIS data obtained primarily during the postnoon local time do not allow for such an analysis, there appears to be a systematic difference between MAVEN electron densities measured in the prenoon and postnoon local time sector (Benna et al., 2015; Fowler et al., 2015; Němec et al., 2017). We have thus plotted the results obtained for the Mars-centered solar orbital (MSO) local time interval 6–12 hr ("morning") by the blue line, and the results obtained for the MSO local time interval 12–18 hr ("afternoon") by the red line. The blue- and red-dashed vertical lines correspond to the respective median values, being equal to about 0.62 and 0.70.

Finally, we verify the model performance using electron densities obtained by radio occultation measurements. The results of this comparison are shown in Figure 11. The used format is the same as in Figure 10. Although radio occultation measurements provide us in principle with entire electron density profiles, their altitudinal extent varies from profile to profile, and using the same comparison procedure as before thus appears reasonable. Figure 11a reveals that the model electron densities are well correlated with measured electron densities (correlation coefficient about 0.95). A distribution of the ratios between the measured and model electron densities depicted in Figure 11b shows that the model densities are typically somewhat larger than the observed electron densities, but the difference is noticeably lower than in the aforementioned case of MAVEN LPW electron density measurements. The median density ratios are about 0.90 and 0.81 during the morning and afternoon local time intervals, respectively. It is noteworthy that the difference between the two local time sectors is opposite as compared to MAVEN LPW electron density measurements.

7. Discussion

Electron density profiles obtained by the MARSIS topside ionospheric sounding are unique in their coverage, spanning over more than 10 years, and, most importantly, all the altitudes from the spacecraft down to the altitude of the peak electron density. An unfortunate drawback of these data is that, due to the low power radiated by MARSIS at low frequencies, low density parts of electron density profiles (up to about 10^4 cm^{-3}, see Němec et al., 2010) are not detected by the radar sounding. Additionally, due to the ionospheric trace inversion procedure (Morgan et al., 2013), the low density (high altitude) part of an electron density profile necessarily affects also the electron density profile at larger densities (lower altitudes). The inversion of MARSIS ionospheric traces is thus intrinsically ambiguous, and different electron density profiles are obtained depending on the assumed electron density profile shape at low densities undetectable by the radar sounding. There are two basic options which allow us to minimize related errors and obtain reliable electron density profiles: (i) A realistic shape of the electron density profile in the region unaccessible
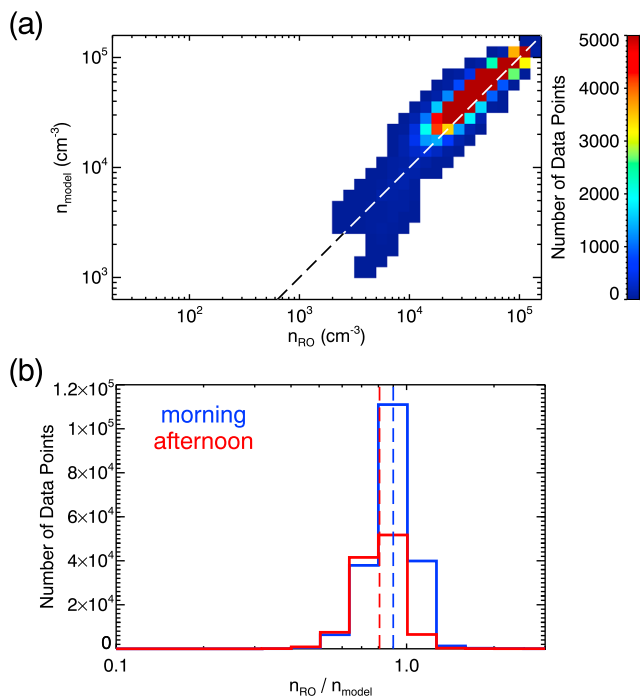
Figure 11. (a) Comparison of model electron densities and electron densities obtained from radio occultation measurements. Number of data points in individual logarithmically sized bins is color coded according to the color scale on the right. The black/white-dashed line shows a 1:1 dependence. (b) Histograms of the ratios between electron densities obtained from radio occultation measurements and model electron densities. The blue and red histograms correspond to the morning and afternoon local time sectors, respectively. The blue- and red-dashed vertical lines correspond to the median values.

by the ionospheric sounding can be employed (Němec, Morgan, & Gurnett, 2016; Němec et al., 2017). (ii) Only electron density profiles obtained at not too high spacecraft altitudes can be used. The lower the altitude threshold is set, the smaller is the altitudinal region where an electron density profile shape cannot be determined from the sounding but has to be assumed. On the other hand, the number of available electron density profiles decreases accordingly. One thus has to look for a compromise between the precision of the profiles and the amount of available data. The altitude threshold in the present study was set to 425 km, that is, only electron density profiles measured at spacecraft altitudes between 325 and 425 km were considered. Although this is somewhat lower than the altitude threshold formerly considered (Němec et al., 2017), it still leaves us with more than 15,000 profiles for the analysis, and it appears to be a reasonable choice for our study.

We have followed the procedure developed by Nsumei et al. (2012) for the case of the Earth's ionosphere which involves the usage of the shape function to accurately describe electron density profile shapes above the peak altitude, and we have shown that it can be readily applied to the Martian dayside ionosphere. Consequently, each topside electron density profile can be characterized by only five parameters: peak electron density and altitude, steepness of the profile at high altitudes, main layer thickness, and a transition altitude. The subsequent identification of relevant controlling factors for each of these parameters, and a related linear regression analysis, allowed us to determine empirical relations describing each of the parameters as a function of SZA, $F10.7$ index, Sun-Mars distance, and crustal magnetic field magnitude. For a given combination of controlling factors, the five parameters describing the electron density profile can be thus readily determined, and these can be, in turn, used to evaluate the electron density profile. We note that while the fitting of individual density profiles is very successful, the subsequent characterization of individual parameters is less successful, possibly suggesting that one parameter can be overcompensated by another one in the model.

The form adopted for the shape function allows the equation (2) to be analytically integrated, so that the reconstruction of electron density profiles is computationally very fast and the model can be straightforwardly and easily implemented. The model performance on the MARSIS radar sounding data which were used for its construction is well satisfactory, with the electron density deviations typically within about 1.5 dB (30–40%) and, most importantly, with principally no systematic bias toward lower or larger electron densities. This appears to be a significant improvement as compared to our former empirical model of electron densities in the dayside ionosphere (Němec et al., 2011; Němec, Morgan, Gurnett, & Andrews, 2016), which when validated using the recent data set appears to systematically overestimate the electron densities. This is likely related to the fact that the model was developed using an older radar sounding data set based on the older version of the trace inversion routine, which was shown to overestimate electron densities due to unrealistic electron density profile shapes assumed in the radar sounding gap region (Němec, Morgan, & Gurnett, 2016). Moreover, the profile shape in the transition region was in this model determined somewhat arbitrarily, with the transition region possibly assumed to be located too high in altitude and too spatially extended, again resulting in the overestimation of model electron densities.

A direct comparison of $F10.7$ values obtained for Mars with the total solar irradiance derived using MAVEN EUV measurements revealed that their correlation is as high as about 0.96, justifying the usage of $F10.7$ index in empirical relations (6)–(10). Additionally, we have assumed that the parameters characterizing the profile shape depend linearly on the envisaged controlling factors. This was necessary in order to simplify the situation by allowing for a linear regression analysis. Although this linear dependence may be at times questionable, it can be more or less justified by a reasonable transformation of the used controlling factors. Additionally, the absolute values of rank correlations between the resulting residuals and all of the considered

controlling factors were lower than 0.1, demonstrating that there are no systematic trends remaining in the data when the suggested parametrization is used.

The validation of the model using independent data sets is particularly important in order to eliminate a possibility of biases stemming from potential problems contained in the original MARSIS radar sounding data set. The electron densities locally evaluated from electron plasma oscillations excited by the MARSIS radar sounding are limited by the spacecraft periapsis to altitudes higher than about 275 km, but they represent arguably the most precise electron density data set available (Duru et al., 2008). The obtained results show that the median ratio of observed to model electron densities is very close to 1, and there thus appears to be no systematic bias. As for the large scatter of the ratios, this is likely related to intrinsic turbulence-like variability of electron densities (Andrews, Andersson, et al., 2015; Gurnett et al., 2010; Wang et al., 2012). While model electron densities at the analyzed altitudes (<325 km) are principally always larger than about $10^3 \, \mathrm{cm}^{-3}$, in agreement with formerly reported statistical results (Andrews, Edberg, et al., 2015; Duru et al., 2008; Němec et al., 2011), the observed electron densities may be as low as $\approx 10 \, \mathrm{cm}^{-3}$. This electron density variability, spanning—under apparently principally the same conditions—over several orders of magnitude is, in particular at higher altitudes, quite striking (Andrews, Andersson, et al., 2015; Gurnett et al., 2010) and nearly impossible to incorporate in the model.

Model electron densities correlate well with electron densities measured by the LPW instrument on board the MAVEN spacecraft. The aforementioned low density tail of the observed electron densities occurs primarily at higher altitudes, where the plasma dynamics is important and in situ measured electron densities can be often significantly lower than the model ones. This is understandable since both the model and the trace inversion assume the density to monotonically increase with decreasing altitude, while in situ measurements can observe density fluctuations and layering of the ionosphere. Consequently, the wave group velocity used in the trace inversion may be underestimated, resulting in a possible overestimation of calculated corrected altitudes. Overall, MAVEN LPW electron densities are systematically lower than the model electron densities, typically by about 30–40%. A comparable median electron density difference of about 27% was reported by Němec et al. (2017) for the four Mars Express–MAVEN conjunction events (within 5° SZA interval and within 1 hr) they analyzed, suggesting that it is likely an instrumental issue rather than the problem of the model formulation itself. A comparison of model electron densities with electron densities obtained by radio occultation measurements reveals that radio occultation measurements are somewhere in the middle, being typically lower than the model electron densities by only about 10–20%. Taking into account that the model results agree well with the electron densities locally evaluated by MARSIS at altitudes above about 275 km, and considering that these are possibly precise to within about 2% (Duru et al., 2008), our results would suggest that the model densities at high altitudes are likely unbiased. The apparent overall overestimation of model electron densities might be then possibly partly related to the aforementioned trace inversion issues. The noticeably lower MAVEN LPW electron densities observed over the entire analyzed altitudinal range could indicate that the problem might be also on the side of LPW electron density measurements. However, one needs to consider that the time interval covered by the MAVEN LPW electron density measurements is quite different than the time interval covered by the MARSIS radar sounding data used to construct the model. This means that MAVEN typically sampled the ionosphere under different solar wind parameters, which may possibly have a significant influence unaccounted for in our model formulation (Sánchez-Cano et al., 2015). Finally, the used radio occultation measurements are significantly limited in SZA, covering principally the very edge of the SZA interval considered in the model formulation. A deteriorated model performance for such extreme parameters may be expected.

8. Conclusions

We used more than 10 years of data obtained by the MARSIS radar sounder on board the Mars Express spacecraft to construct an empirical model of the Martian topside ionosphere at SZAs lower than 80°. The analysis was limited to the altitudes lower than 325 km, where the electron densities are large enough to be adequately measured by the MARSIS radar sounding. Altogether, 16,044 electron density profiles obtained at spacecraft altitudes lower than 425 km and SZAs lower than 80° were included in the analysis. An improved trace inversion method was applied to obtain the most reliable electron density profiles available. We have shown that each of the measured electron density profiles can be accurately characterized by five parameters: the peak electron density and peak altitude, steepness at high altitudes α, main layer thickness β, and transition altitude h_T. We further investigated how these parameters vary with relevant controlling factors,

revealing their statistical dependences. MAVEN EUV data were used to show that the solar ionizing flux can be accurately approximated by the F10.7 index when taking into account the solar rotation. The obtained dependences represent a formulation of a simple and readily usable empirical model of electron densities in the Martian dayside upper ionosphere. The performance of this model was tested using three independent data sets: (i) electron densities locally evaluated based on plasma oscillations excited by the MARSIS radar sounding, (ii) electron densities measured in situ by the LPW instrument on board the MAVEN spacecraft, and (iii) electron densities obtained by radio occultation measurements. The electron densities measured by MAVEN are systematically lower than those predicted by the model, in agreement with formerly analyzed conjunction events (Němec et al., 2017). Overall, the model appears to express main electron density trends and to perform reasonably well.

References

Andersson, L., Ergun, R. E., Delory, G. T., Eriksson, A., Westfall, J., Reed, H., et al. (2015). The Langmuir Probe and Waves (LPW) instrument for MAVEN. *Space Science Reviews*, *195*, 173–198. https://doi.org/10.1007/s11214-015-0194-3

Andrews, D. J., Andersson, L., Delory, G. T., Ergun, R. E., Eriksson, A. I., Fowler, C. M., et al. (2015). Ionospheric plasma density variations observed at Mars by MAVEN/LPW. *Geophysical Research Letters*, *42*, 8862–8869. https://doi.org/10.1002/2015GL065241

Andrews, D. J., André, M., Opgenoorth, H. J., Edberg, N. J. T., Diéval, C., Duru, F., et al. (2014). Oblique reflections in the Mars Express MARSIS data set: Stable density structures in the Martian ionosphere. *Journal of Geophysical Research: Space Physics*, *119*, 3944–3960. https://doi.org/10.1002/2013JA019697

Andrews, D. J., Edberg, N. J. T., Eriksson, A. I., Gurnett, D. A., Morgan, D., Němec, F., & Opgenoorth, H. J. (2015). Control of the topside Martian ionosphere by crustal magnetic fields. *Journal of Geophysical Research: Space Physics*, *120*, 3042–3058. https://doi.org/10.1002/2014JA020703

Andrews, D. J., Opgenoorth, H. J., Edberg, N. J. T., André, M., Fränz, M., Dubinin, E., et al. (2013). Determination of local plasma densities with the MARSIS radar: Asymmetries in the high-altitude Martian ionosphere. *Journal of Geophysical Research: Space Physics*, *118*, 6228–6242. https://doi.org/10.1002/jgra.50593

Benna, M., Mahaffy, P. R., Grebowsky, J. M., Fox, J. L., Yelle, R. V., & Jakosky, B. M. (2015). First measurements of composition and dynamics of the Martian ionosphere by MAVEN's neutral gas and ion spectrometer. *Geophysical Research Letters*, *42*, 8958–8965. https://doi.org/10.1002/2015GL066146

Cain, J. C., Ferguson, B. B., & Mozzoni, D. (2003). An n = 90 internal potential function of the Martian crustal magnetic field. *Journal of Geophysical Research*, *108*(E2), 5008. https://doi.org/10.1029/2000JE001487

Chapman, S. (1931a). The absorption and dissociative or ionizing effect of monochromatic radiation in an atmosphere on a rotating Earth. *Proceedings of the Physical Society*, *43*, 26–45. https://doi.org/10.1088/0959-5309/43/1/305

Chapman, S. (1931b). The absorption and dissociative or ionizing effect of monochromatic radiation in an atmosphere on a rotating Earth, Part II. Grazing incidence. *Proceedings of the Physical Society*, *43*, 483–501. https://doi.org/10.1088/0959-5309/43/5/302

Chaufray, J. Y., Gonzalez-Galindo, F., Forget, F., Lopez-Valverde, M., Leblanc, F., Modolo, R., et al. (2014). Three-dimensional Martian ionosphere model: II. Effect of transport processes due to pressure. *Journal of Geophysical Research: Planets*, *119*, 1614–1636. https://doi.org/10.1002/2013JE004551

Dubinin, E., Fraenz, M., Andrews, D., & Morgan, D. (2016). Martian ionosphere observed by Mars Express. 1. Influence of the crustal magnetic fields. *Planetary and Space Science*, *125*, 62–75. https://doi.org/10.1016/j.pss.2016.02.004

Duru, F., Gurnett, D. A., Morgan, D. D., Modolo, R., Nagy, A. F., & Najib, D. (2008). Electron densities in the upper ionosphere of Mars from the excitation of electron plasma oscillations. *Journal of Geophysical Research*, *113*, A07302. https://doi.org/10.1029/2008JA013073

Duru, F., Morgan, D. D., & Gurnett, D. A. (2010). Overlapping ionospheric and surface echoes observed by the Mars Express radar sounder near the martian terminator. *Geophysical Research Letters*, *37*, L23102. https://doi.org/10.1029/2010GL045859

Eparvier, F. G., Chamberlin, P. C., Woods, T. N., & Thiemann, E. M. B. (2015). The solar extreme ultraviolet monitor for MAVEN. *Space Science Reviews*, *195*(1–4), 293–301. https://doi.org/10.1007/s11214-015-0195-2

Fallows, K., Withers, P., & Matta, M. (2015a). An observational study of the influence of solar zenith angle on properties of the M1 layer of the Mars ionosphere. *Journal of Geophysical Research: Space Physics*, *120*, 1299–1310. https://doi.org/10.1002/2014JA020750

Fallows, K., Withers, P., & Matta, M. (2015b). Numerical simulations of the influence of solar zenith angle on properties of the M1 layer of the Mars ionosphere. *Journal of Geophysical Research: Space Physics*, *120*, 6707–6721. https://doi.org/10.1002/2014JA020947

Flynn, C. L., Vogt, M. F., Withers, P., Andersson, L., England, S., & Liu, G. (2017). MAVEN observations of the effects of crustal magnetic fields on electron density and temperature in the Martian dayside ionosphere. *Geophysical Research Letters*, *44*, 10,812–10,821. https://doi.org/10.1002/2017GL075367

Fowler, C. M., Andersson, L., Ergun, R. E., Morooka, M., Delory, G., Andrews, D. J., et al. (2015). The first in situ electron temperature and density measurements of the Martian nightside ionosphere. *Geophysical Research Letters*, *42*, 8854–8861. https://doi.org/10.1002/2015GL065267

Fox, J. L., & Weber, A. J. (2012). MGS electron density profiles: Analysis and modeling of peak altitudes. *Icarus*, *221*, 1002–1019. https://doi.org/10.1016/j.icarus.2012.10.002

Fox, J. L., & Yeager, K. E. (2009). MGS electron density profiles: Analysis of the peak magnitudes. *Icarus*, *200*, 468–479. https://doi.org/10.1016/j.icarus.2008.12.002

Girazian, Z., & Withers, P. (2013). The dependence of peak electron density in the ionosphere of Mars on solar irradiance. *Geophysical Research Letters*, *40*, 1960–1964. https://doi.org/10.1002/grl.50344

Gonzalez-Galindo, F., Chaufray, J.-Y., Lopez-Valverde, M. A., Gilli, G., Forget, F., Leblanc, F., et al. (2013). Three-dimensional Martian ionosphere model: I. The photochemical ionosphere below 180 km. *Journal of Geophysical Research: Planets*, *118*, 2105–2123. https://doi.org/10.1002/jgre.20150

Grandin, M., Blelly, P.-L., Witasse, O., & Marchaudon, A. (2014). Mars Express radio-occultation data: A novel analysis approach. *Journal of Geophysical Research: Space Physics*, *119*, 10,621–10,632. https://doi.org/10.1002/2014JA020698

Gurnett, D. A., Huff, R. L., Morgan, D. D., Persoon, A. M., Averkamp, T. F., Kirchner, D. L., et al. (2008). An overview of radar soundings of the Martian ionosphere from the Mars Express spacecraft. *Advances in Space Research*, *41*, 1335–1346. https://doi.org/10.1016/j.asr.2007.01.062

Gurnett, D. A., Kirchner, D. L., Huff, R. L., Morgan, D. D., Persoon, A. M., Averkamp, T. F., et al. (2005). Radar soundings of the ionosphere of Mars. *Science*, *310*, 1929–1933. https://doi.org/10.1126/science.1121868

Gurnett, D. A., Morgan, D. D., Duru, F., Akalin, F., Winningham, D., Frahm, R. A., et al. (2010). Large density fluctuations in the Martian ionosphere as observed by the Mars Express radar sounder. *Icarus*, *206*(1), 83–94. https://doi.org/10.1016/j.icarus.2009.02.019

Hanson, W. B., & Zuccaro, D. R. (1977). The Martian ionosphere as observed by the Viking retarding potential analyzers. *Journal of Geophysical Research*, *82*(28), 4351–4363. https://doi.org/10.1029/JS082i028p04351

Hantsch, M. H., & Bauer, S. J. (1990). Solar control of the Mars ionosphere. *Planetary and Space Science*, *38*(4), 539–542. https://doi.org/10.1016/0032-0633(90)90146-H

Hinson, D. P., Simpson, R. A., Twicken, J. D., Tyler, G. L., & Flasar, F. M. (1999). Initial results from radio occultation measurements with Mars Global Surveyor. *Journal of Geophysical Research*, *104*(E11), 26,997–27,012. https://doi.org/10.1029/1999JE001069

Jakosky, B. M., Lin, R. P., Grebowsky, J. M., Luhmann, J. G., Mitchell, D. F., Beutelschies, G., et al. (2015). The Mars Atmosphere and Volatile Evolution (MAVEN) mission. *Space Science Reviews*, *195*(1), 3–48. https://doi.org/10.1007/s11214-015-0139-x

Jordan, R., Picardi, G., Plaut, J., Wheeler, K., Kirchner, D., Safaeinili, A., et al. (2009). The Mars Express MARSIS sounder instrument. *Planetary and Space Science*, *57*, 1975–1986. https://doi.org/10.1016/j.pss.2009.09.016

Kliore, A. J., Cain, D. L., Fjeldbo, G., Seidel, B. L., & Rasool, S. I. (1972a). Mariner 9 S-band Martian occultation experiment: Initial results on the atmosphere and topography of Mars. *Science*, *175*(4019), 313–317. https://doi.org/10.1126/science.175.4019.313

Kliore, A. J., Cain, D. L., Fjeldbo, G., Seidel, B. L., Sykes, M. J., & Rasool, S. I. (1972b). The atmosphere of Mars from Mariner 9 radio occultation measurements. *Icarus*, *17*, 484–516. https://doi.org/10.1016/0019-1035(72)90014-0

Mahaffy, P. R., Benna, M., King, T., Harpold, D. N., Arvey, R., Barciniak, M., et al. (2015). The neutral gas and ion mass spectrometer on the Mars Atmosphere and Volatile Evolution Mission. *Space Science Reviews*, *195*(1–4), 49–73. https://doi.org/10.1007/s11214-014-0091-1

Matta, M., Mendillo, M., Withers, P., & Morgan, D. (2015). Interpreting Mars ionospheric anomalies over crustal magnetic field regions using a 2-D ionospheric model. *Journal of Geophysical Research: Space Physics*, *120*, 766–777. https://doi.org/10.1002/2014JA020721

Mendillo, M., Marusiak, A. G., Withers, P., Morgan, D., & Gurnett, D. (2013). A new semiempirical model of the peak electron density of the Martian ionosphere. *Geophysical Research Letters*, *40*, 5361–5365. https://doi.org/10.1002/2013GL057631

Mendillo, M., Narvaez, C., Trovato, J., Withers, P., Mayyasi, M., Morgan, D., et al. (2018). Mars Initial Reference Ionosphere (MIRI) model: Updates and validations using MAVEN, MEX, and MRO data sets. *Journal of Geophysical Research: Space Physics*, *123*, 5674–5683. https://doi.org/10.1029/2018JA025263

Mendillo, M., Narvaez, C., Vogt, M. F., Mayyasi, M., Forbes, J., Galand, M., et al. (2017a). Sources of ionospheric variability at Mars. *Journal of Geophysical Research: Space Physics*, *122*, 9670–9684. https://doi.org/10.1002/2017JA024366

Mendillo, M., Narvaez, C., Vogt, M. F., Mayyasi, M., Mahaffy, P., Benna, M., et al. (2017b). MAVEN and the total electron content of the Martian ionosphere. *Journal of Geophysical Research: Space Physics*, *122*, 3526–3537. https://doi.org/10.1002/2016JA023474

Morgan, D. D., Gurnett, D. A., Kirchner, D. L., Fox, J. L., Nielsen, E., & Plaut, J. J. (2008). Variation of the Martian ionospheric electron density from Mars Express radar soundings. *Journal of Geophysical Research*, *113*, A09303. https://doi.org/10.1029/2008JA013313

Morgan, D. D., Witasse, O., Nielsen, E., Gurnett, D. A., Duru, F., & Kirchner, D. L. (2013). The processing of electron density profiles from the Mars Express MARSIS topside sounder. *Radio Science*, *48*, 197–207. https://doi.org/10.1002/rds.20023

Němec, F., Morgan, D. D., Fowler, C., Kopf, A. J., Andersson, L., Gurnett, D. A., et al. (2017). Ionospheric electron densities at Mars: Comparison of Mars Express ionospheric sounding and MAVEN local measurements. *Journal of Geophysical Research: Space Physics*, *122*, 12,393–12,405. https://doi.org/10.1002/2017JA024629

Němec, F., Morgan, D. D., & Gurnett, D. A. (2016). On improving the accuracy of electron density profiles obtained at high altitudes by the ionospheric sounder on the Mars Express spacecraft. *Journal of Geophysical Research: Space Physics*, *121*, 10,117–10,129. https://doi.org/10.1002/2016JA023054

Němec, F., Morgan, D. D., Gurnett, D. A., & Andrews, D. J. (2016). Empirical model of the Martian dayside ionosphere: Effects of crustal magnetic fields and solar ionizing flux at higher altitudes. *Journal of Geophysical Research: Space Physics*, *121*, 1760–1771. https://doi.org/10.1002/2015JA022060

Němec, F., Morgan, D. D., Gurnett, D. A., & Duru, F. (2010). Nightside ionosphere of Mars: Radar soundings by the Mars Express spacecraft. *Journal of Geophysical Research*, *115*, E12009. https://doi.org/10.1029/2010JE003663

Němec, F., Morgan, D. D., Gurnett, D. A., Duru, F., & Truhlík, V. (2011). Dayside ionosphere of Mars: Empirical model based on data from the MARSIS instrument. *Journal of Geophysical Research*, *116*, E07003. https://doi.org/10.1029/2010JE003789

Nielsen, E., Zou, H., Gurnett, D. A., Kirchner, D. L., Morgan, D. D., Huff, R., et al. (2006). Observations of vertical reflections from the topside Martian ionosphere. *Space Science Reviews*, *126*, 373–388. https://doi.org/10.1007/s11214-006-9113-y

Nsumei, P., Reinisch, B., Huang, X., & Bilitza, D. (2012). New vary-Chap profile of the topside ionosphere electron density distribution for use with the IRI model and the GIRO real time data. *Radio Science*, *47*, RS0L16. https://doi.org/10.1029/2012RS004989

Orosei, R., Jordan, R. L., Morgan, D. D., Cartacci, M., Cicchetti, A., Duru, F., et al. (2015). Mars Advanced Radar for Subsurface and Ionospheric Sounding (MARSIS) after nine years of operation: A summary. *Planetary and Space Science*, *112*, 98–114. https://doi.org/10.1016/j.pss.2014.07.010

Pätzold, M., Tellmann, S., Häusler, B., Hinson, D., Schaa, R., & Tyler, G. L. (2005). A sporadic third layer in the ionosphere of Mars. *Science*, *310*, 837–839. https://doi.org/10.1126/science.1117755

Picardi, G., Biccari, D., Seu, R., Plaut, J., Johnson, W. T. K., Safaeinili, R. L. J. A., et al. (2004). MARSIS: Mars Advanced Radar for Subsurface and Ionosphere Sounding. In A. Wilson & A. Chicarro (Eds.), *Mars Express: The scientific payload, ESA Special Publication* (Vol. 1240, pp. 51–69). Noordwijk, Netherlands: ESTEC.

Rao, N. V., Balan, N., & Patra, A. K. (2014). Solar rotation effects on the Martian ionosphere. *Journal of Geophysical Research: Space Physics*, *119*, 6612–6622. https://doi.org/10.1002/2014JA019894

Reinisch, B. W., Huang, X.-Q., Belehaki, A., Shi, J.-K., Zhang, M.-L., & Ilma, R. (2004). Modelling the IRI topside profile using scale heights from ground-based ionosonde measurements. *Advances in Space Research*, *34*, 2026–2031. https://doi.org/10.1016/j.asr.2004.06.012

Reinisch, B. W., Nsumei, P., Huang, X., & Bilitza, D. K. (2007). Modelling the F2 topside and plasmasphere for IRI using IMAGE/RPI and ISIS data. *Advances in Space Research*, *39*, 731–738. https://doi.org/10.1016/j.asr.2006.05.032

Safaeinili, A., Kofman, W., Mouginot, J., Gim, Y., Herique, A., Ivanov, A. B., et al. (2007). Estimation of the total electron content of the Martian ionosphere using radar sounder surface echoes. *Geophysical Research Letters*, *34*, L23204. https://doi.org/10.1029/2007GL032154

Sánchez-Cano, B., Lester, M., Witasse, O., Milan, S. E., Hall, B. E. S., Blelly, P.-L., et al. (2015). Evidence of scale height variations in the Martian ionosphere over the solar cycle. *Journal of Geophysical Research: Space Physics*, *120*, 10,913–10,925. https://doi.org/10.1002/2015JA021949

Sánchez-Cano, B., Radicella, S. M., Herraiz, M., Witasse, O., & Rodríguez-Caderot, G. (2013). NeMars: An empirical model of the martian dayside ionosphere based on Mars Express MARSIS data. *Icarus*, *225*, 236–247. https://doi.org/10.1016/j.icarus.2013.03.021

Thiemann, E. M. B., Chamberlin, P. C., Eparvier, F. G., Templeman, B., Woods, T. N., Bougher, S. W., & Jakosky, B. M. (2017). The MAVEN EUVM model of solar spectral irradiance variability at Mars: Algorithms and results. *Journal of Geophysical Research: Space Physics*, *122*, 2748–2767. https://doi.org/10.1002/2016JA023512

Triskova, L., Galkin, I., Truhlik, V., & Reinisch, B. W. (2007). Application of seamless vertical profiles for use in the topside electron density modeling. *Advances in Space Research*, *39*, 774–778. https://doi.org/10.1016/j.asr.2006.09.033

Tyler, G. L., Balmino, G., Hinson, D. P., Sjogren, W. L., Smith, D. E., Simpson, R. A., et al. (2001). Radio science observations with Mars Global Surveyor: Orbit insertion through one Mars year in mapping orbit. *Journal of Geophysical Research*, *106*(E10), 23,327–23,348. https://doi.org/10.1029/2000JE001348

Vogt, M. F., Withers, P., Fallows, K., Andersson, L., Girazian, Z., Mahaffy, P. R., et al. (2017). MAVEN observations of dayside peak electron densities in the ionosphere of Mars. *Journal of Geophysical Research: Space Physics*, *122*, 891–906. https://doi.org/10.1002/2016JA023473

Vogt, M. F., Withers, P., Fallows, K., Flynn, C. L., Andrews, D. J., Duru, F., & Morgan, D. D. (2016). Electron densities in the ionosphere of Mars: A comparison of MARSIS and radio occultation measurements. *Journal of Geophysical Research: Space Physics*, *121*, 10,241–10,257. https://doi.org/10.1002/2016JA022987

Wang, X.-D., Wang, J.-S., & Zou, H. (2012). On the small-scale fluctuations in the peak electron density of Martian ionosphere observed by MEX/MARSIS. *Planetary and Space Science*, *63–64*, 87–93. https://doi.org/10.1016/j.pss.2011.10.007

Withers, P. (2009). A review of observed variability in the dayside ionosphere of Mars. *Advances in Space Research*, *44*, 277–3078. https://doi.org/10.1016/j.asr.2009.04.027

Withers, P., Felici, M., Mendillo, M., Moore, L., Narvaez, C., Vogt, M. F., & Jakosky, B. M. (2018). First ionospheric results from the MAVEN Radio Occultation Science Experiment (ROSE). *Journal of Geophysical Research: Space Physics*, *123*, 4171–4180. https://doi.org/10.1029/2018JA025182

Withers, P., Mendillo, M., Rishbeth, H., Hinson, D. P., & Arkani-Hamed, J. (2005). Ionospheric characteristics above Martian crustal magnetic anomalies. *Geophysical Research Letters*, *32*, L16204. https://doi.org/10.1029/2005GL023483

Withers, P., Morgan, D. D., & Gurnett, D. A. (2015). Variations in peak electron densities in the ionosphere of Mars over a full solar cycle. *Icarus*, *251*, 5–11. https://doi.org/10.1016/j.icarus.2014.08.008

Withers, P., Vogt, M., Mahaffy, P., Benna, M., Elrod, M., & Jakosky, B. (2015). Changes in the thermosphere and ionosphere of Mars from Viking to MAVEN. *Geophysical Research Letters*, *42*, 9071–9079. https://doi.org/10.1002/2015GL065985

Withers, P., Weiner, S., & Ferreri, N. R. (2015). Recovery and validation of Mars ionospheric electron density profiles from Mariner 9. *Earth, Planets and Space*, *67*, 194. https://doi.org/10.1186/s40623-015-0364-2